

# Phase control of local and non-local entanglement in a triple spin qubit

Takashi Nakajima<sup>1</sup>, Matthieu R. Delbecq<sup>1</sup>, Tomohiro Otsuka<sup>1</sup>, Shinichi Amaha<sup>1</sup>, Jun Yoneda<sup>1</sup>, Akito Noiri<sup>2</sup>, Kenta Takeda<sup>1</sup>, Giles Allison<sup>1</sup>, Arne Ludwig<sup>3</sup>, Andreas D. Wieck<sup>3</sup>, & Seigo Tarucha<sup>1,2</sup>

<sup>1</sup>*Center for Emergent Matter Science, RIKEN, 2-1 Hirosawa, Wako-shi, Saitama 351-0198, Japan*

<sup>2</sup>*Department of Applied Physics, University of Tokyo, 7-3-1 Hongo, Bunkyo-ku, Tokyo 113-8656, Japan*

<sup>3</sup>*Lehrstuhl für Angewandte Festkörperphysik, Ruhr-Universität Bochum, D-44780 Bochum, Germany*

**Entanglement is at the heart of quantum mechanics and an essential ingredient of spin correlations in superconductivity and the Kondo effect and quantum non-locality of non-interacting particles<sup>1–4</sup>. Non-local entanglement is also key to quantum computation outperforming classical computers<sup>5</sup> and has now begun to be applied to various atom and photon-based quantum information technologies<sup>6</sup>. Despite many technical advances in manipulating electron spins in solids, entanglement control has only been realized for two coupled qubits in quantum dots (QDs), mainly by local SWAP operations<sup>7–11</sup>. Here we use a triple QD with three addressable spin qubits to demonstrate phase control of locally entangled two or three electron spins and two non-locally entangled uncoupled spins. Singlet-triplet oscillation of two locally entangled spins in adjacent dots is induced by a built-in local Zeeman field, and phase-modulated using the exchange-coupled third spin as a control bit. Non-local entangle-**

**ment is created by an adiabatic transition from the local singlet to a non-local singlet over two distant QDs with the center dot remaining uncoupled. We analyze the phase evolution of those entangled states depending on the adiabatic transition path to derive the three-spin-state spectrum, a prerequisite for single-qubit<sup>12-14</sup>, SWAP gate<sup>8,9</sup> and other entanglement operations. Our results empower quantum information technologies in solid-state systems by paving the way for manipulating local and non-local entanglement with multiple QDs.**

To address and manipulate individual entangled electronic states in solid-state systems is a fundamental requirement for quantum information processing and it has been facilitated by using confined electron spins in semiconductor QDs, i.e., singlet and a triplet in double QDs (DQDs), and doublets and a quadruplet in triple QDs (TQDs)<sup>15-17</sup>. Combining manipulations of these entangled states with single spin rotation gates enables a universal set of quantum logic gates<sup>18</sup>, thus making the QD-based architecture a promising building block for quantum information processing. To date, numerous efforts have been made to implement entangling gates using exchange coupling<sup>8,9,19</sup>, capacitive coupling<sup>20</sup>, and superexchange coupling via a mediator QD<sup>10,11</sup>. However, all of them rely on the direct interaction between two locally coupled qubits, although non-locality or correlation between uncoupled particles is the most intriguing concept of entanglement. Control of entanglement between three or more qubits remains a great challenge because of the demanding requirements involved: one has to control at least two exchange couplings while keeping the addressability of single-qubit operations. In this Letter, we employ a three-qubit system realized in a TQD to generate and control local and non-local two-spin entanglements and three-spin entanglement. We first demonstrate single-qubit operations and SWAP gate operations in two

pairs of nearest neighbor spins in the TQD. Then we observe the singlet-triplet (S-T) oscillation of two adjacent spins governed by the local Zeeman splitting created by a micromagnet (MM). We find that the phase of the S-T oscillation is controlled by the state of the exchange-coupled third spin, which can be used for CPHASE gate operations between different kinds of qubit subspaces<sup>21</sup>. By using the adiabatic transition through the three-spin energy diagram in the TQD, we also find a non-locally entangled state is generated in the spins at both ends of the TQD that have no direct exchange coupling with each other. Through analysis of the S-T oscillations depending on the adiabatic transition point, we derive the three-spin spectrum in the TQD with the finite local Zeeman fields and the exchange couplings. This spectrum can be used to choose the operation conditions for various single-qubit and entangling gates in multi-qubit devices.

In TQDs with finite exchange couplings, three electron spins comprise a quadruplet and two doublets. While these composite spin states provide a platform for the exchange-only qubit<sup>22, 23</sup>, individual access to single spin states is not feasible in this regime. We place a cobalt MM on top of our gate-defined TQD in a GaAs/AlGaAs heterostructure to induce an inhomogeneous Zeeman field along the externally applied in-plane magnetic field  $B_{\text{ext}}$  (Fig. 1a)<sup>24, 25</sup>. The Zeeman energy difference  $\Delta B_{ij}$  between QD*i* and QD*j* (*i*, *j* = 1, 2, 3) splits the energy of the degenerate three-spin states with the same *z* component of total spin  $S_z$  as shown in Fig. 1b. This allows us to control each single spin when  $\Delta B_{ij}$  is sufficiently larger than the exchange coupling energy  $J_{ij}$  ( $|\Delta B_{ij}/J_{ij}| \gg 1$ ). In this regime, the three-spin eigenstates are described by  $|\sigma_1\sigma_2\sigma_3\rangle = |\sigma_1\rangle \otimes |\sigma_2\rangle \otimes |\sigma_3\rangle$  ( $\sigma_i = \uparrow, \downarrow$ ) rather than the quadruplet and doublets. The charge configuration in the TQD is probed using a nearby rf-QD charge sensor (see Methods) and the number of electrons

in each QD,  $N_i$ , is counted by varying the gate biases P1 and P3 applied to two of the plunger gates. The following experiments are performed in the  $(N_1 N_2 N_3) = (111)$  charge configuration shown in Fig. 1c, unless otherwise noted. For the qubit initialization, operation and measurement, voltage pulses are superposed onto P1 and P3 to control the detuning energy  $\varepsilon$  between (102) and (201). With the energy diagram in Fig. 1b established experimentally, we can readily implement single-qubit and two-qubit gate operations to realize a full three-spin qubit architecture.

Coherent rotations of each spin qubit (Fig. 1d) is observed by preparing one of the eigenstates of the local Zeeman field at  $\varepsilon = 0$ ,  $|\sigma_1 \downarrow_2 \uparrow_3\rangle$  or  $|\downarrow_1 \uparrow_2 \sigma_3\rangle$ , and driving the electron spin resonance (ESR) with the MM proximity field and a microwave burst (See Ref. <sup>26</sup> and Methods for details). The spin rotations are detected by the singlet return probability  $P_S$  inferred from repetitive single-shot measurement. This result clearly demonstrates addressable control of the three spin qubits Q1-3.

Two-qubit SWAP gate operations are demonstrated in Fig. 1e. The spin states are first initialized in (102), where two electrons in the right QD occupy the singlet ground state,  $S_3$ . The electron in the left QD is left uninitialized and therefore its spin state is thermally populated with the Boltzmann distribution. Thus the initial state of the system is described by the density matrix of a mixed state,  $\rho_0 = \alpha |\uparrow_1 S_3\rangle \langle \uparrow_1 S_3| + (1 - \alpha) |\downarrow_1 S_3\rangle \langle \downarrow_1 S_3|$ , with  $\alpha \approx 0.7$  resulting from the electron temperature in the reservoirs,  $T_e = 240$  mK. The  $|\sigma_1 S_3\rangle$  state is then loaded into  $|\sigma_1 \downarrow_2 \uparrow_3\rangle$  at  $\varepsilon = 0$ , and the detuning is positively (negatively) displaced to turn the exchange coupling  $J_{23}$  ( $J_{12}$ ) on. During the hold time of  $\tau_{\text{SWAP}}$ , qubits Q2 and Q3 (Q1 and Q2) are swapped at frequency

$J(\varepsilon)/h$ . While  $|\sigma_1 \downarrow_2 \uparrow_3\rangle$  is swapped with  $|\sigma_1 \uparrow_2 \downarrow_3\rangle$  by  $J_{23}$  both for  $\sigma_1 = \uparrow$  and  $\downarrow$ , the swap between  $|\sigma_1 \downarrow_2 \uparrow_3\rangle$  and  $|\downarrow_1 \uparrow_2 \uparrow_3\rangle$  by  $J_{12}$  is visible only for  $\sigma_1 = \uparrow$ . Outcomes  $|\sigma_1 \uparrow_2 \downarrow_3\rangle$  and  $|\downarrow_1 \uparrow_2 \uparrow_3\rangle$  are unloaded to one of the triplet states and detected by measuring  $P_S$ .

Now we turn to the generation of entanglement between those qubits. A locally entangled qubit pair is readily generated by rapidly loading  $|\sigma_1 S_3\rangle$  into the (111) charge configuration (see Methods). When  $Q1$  can be neglected, this rapid adiabatic passage loads  $|S_3\rangle$  into a spin singlet between  $Q2$  and  $Q3$ ,  $|S_{23}\rangle = \frac{1}{\sqrt{2}}(|\uparrow_2 \downarrow_3\rangle - |\downarrow_2 \uparrow_3\rangle)$ . The loaded state starts to oscillate with time  $t_{\text{evolve}}$  between  $|S_{23}\rangle$  and  $|T_{23}\rangle = \frac{1}{\sqrt{2}}(|\uparrow_2 \downarrow_3\rangle + |\downarrow_2 \uparrow_3\rangle)$  (spin triplet) reflecting relative phase evolution between  $|\downarrow_2 \uparrow_3\rangle$  and  $|\uparrow_2 \downarrow_3\rangle$  due to the energy difference. The inset of Fig. 2a shows the probability of finding  $S_{23}$  which oscillates with frequency independent of the state of  $Q1$ . However, when  $J_{12}$  is made larger by increasing the left inter-dot tunnel coupling, we find a striking beating pattern as shown in Fig. 2a. This is because the oscillation frequency deviates differently for  $\sigma_1 = \uparrow$  and  $\downarrow$ , and the oscillations with the two different frequencies are superposed when ensemble averaging is performed on the data taken with the initial mixed state  $\rho_0$ . In the limit of small coupling ( $|J_{12}/\Delta B_{12}| \ll 1$ ), this effect is described by the entanglement of  $Q1$  with the  $S_{23}$ - $T_{23}$  qubit subspace through  $J_{12}$ <sup>21</sup>. The effective Hamiltonian is given by  $H_{\text{int}} = \frac{1}{4}J_{12}\boldsymbol{\sigma}_1 \cdot \boldsymbol{\sigma}_{\text{ST}}$  where  $\boldsymbol{\sigma}_1$  and  $\boldsymbol{\sigma}_{\text{ST}}$  are the Pauli vectors for  $Q1$  and the  $S_{23}$ - $T_{23}$  qubit. This allows for a CPHASE gate operation (Fig. 2b) to interchange quantum information between a single-spin qubit and a S-T qubit<sup>21,27</sup>, where the former could be used as a long-coherence memory while the latter could be used for fast gate operations through electric fields.

To further elucidate the effect of the exchange couplings and examine the three-spin eigenenergies as shown in Fig. 1b, we measure similar coherent evolutions at various values of the detuning  $\varepsilon$ . The left panel of Fig. 3a clearly shows that  $P_S$  oscillates with frequency depending on  $\varepsilon$ . We calculate the 1D Fourier transform of the data to derive the energy gaps between two pairs of branches that correspond to  $|\sigma_1 \downarrow_2 \uparrow_3\rangle$  and  $|\sigma_1 \uparrow_2 \downarrow_3\rangle$  at  $\varepsilon \approx 0$  (marked by green arrows in Fig. 1b). As shown in the left panel of Fig. 3b, we find a single spectral peak or energy gap at around  $\varepsilon \gtrsim 0$  which is almost unchanged with  $\varepsilon$ . The oscillation frequency is given by  $\Delta B_{23}/h = 45$  MHz irrespective of the state of Q1 in agreement with the splitting in the ESR spectra (see Methods). Quenching the effect of  $J_{12}$  ( $\ll \Delta B_{12}$ ) is an essential requirement to maintain the phase coherence between Q2 and Q3 during single-qubit operations. The result in Fig. 3b demonstrates that our TQD device satisfies this requirement.

As  $\varepsilon$  becomes more negative, however, we observe clear splitting of the spectral lines because the energy gap becomes larger (smaller) than  $\Delta B_{23}$  for  $\sigma_1 = \uparrow$  ( $\downarrow$ ) due to the effect of  $J_{12}$ . On the other side of positive  $\varepsilon$ , the gap increases equally for both  $\sigma_1 = \uparrow$  and  $\downarrow$  due to the increase of  $J_{23}$ . These  $\varepsilon$  dependencies are strikingly different from those in previously reported TQD devices<sup>22, 23, 28</sup> but well reproduced by the energy diagram calculated for finite local Zeeman fields in Fig. 1b. By fitting the observed spectral lines with the calculated energy gaps for  $\sigma_1 = \uparrow$  and  $\downarrow$  (depicted by red solid and blue dashed lines respectively in Fig. 3b), we can extract all the TQD parameters characterizing the three-spin energies, including the left and right inter-dot tunnel couplings and the local Zeeman field differences, which quantitatively reproduce the data as shown in the right panels of Fig. 3a and 3b (see Methods).

The TQD spectroscopy demonstrated here provides information of appropriate operating conditions for accurate control of the exchange couplings to generate and manipulate a non-locally entangled qubit pair as shown in the inset of Fig. 4a. When  $\varepsilon$  is made more negative away from  $\varepsilon = 0$ ,  $|\uparrow_1\downarrow_2\uparrow_3\rangle$  is adiabatically loaded into a triplet-like state  $|T_{12}\uparrow_3\rangle$  at  $\varepsilon \approx \varepsilon_L$  as  $J_{12}$  is increased. Here the  $|\uparrow_1 S_3\rangle$  state in  $\rho_0$  is transferred to the superposition of  $|\uparrow_1\uparrow_2\downarrow_3\rangle$  and  $|T_{12}\uparrow_3\rangle$ , which suggests generation of a tripartite entangled state known as the W state (see Methods). In the limit of further negative detuning ( $\varepsilon \ll \varepsilon_L$ ),  $|T_{12}\uparrow_3\rangle$  is then loaded into  $|\downarrow_1\uparrow_2\uparrow_3\rangle$ . This process transfers  $|\uparrow_1 S_{23}\rangle$  to  $|\uparrow_2\rangle \otimes |S_{13}\rangle = \frac{1}{\sqrt{2}}(|\uparrow_1\uparrow_2\downarrow_3\rangle - |\downarrow_1\uparrow_2\uparrow_3\rangle)$ , generating the *non-local* entanglement of Q1 and Q3 that have *no* direct interaction with each other. Then the  $S_{13}$ - $T_{13}$  precession starts to occur with a frequency governed by the relevant energy gap approximately given by  $\Delta B_{13} = \Delta B_{12} + \Delta B_{23}$ , which can be clearly distinguished from the  $S_{23}$ - $T_{23}$  precession. The  $S_{13}$  component after the precession is read out by transferring  $|\uparrow_2\rangle \otimes |S_{13}\rangle$  back to  $|\uparrow_1 S_{23}\rangle$  in the reverse process. The observed coherent oscillation at  $\varepsilon \ll \varepsilon_L$  entirely agrees with the calculation in Fig. 4a. From this result we infer the evolution of the Bloch vector in the  $\sigma_2 = \uparrow$  subspace as shown in Figs. 4b-d. We note that the state initialized with  $\sigma_1 = \downarrow$  makes almost no contribution to the observed oscillations because the  $|\downarrow_1\uparrow_2\downarrow_3\rangle$  state at  $\varepsilon = 0$  is unloaded into the (201) charge configuration at  $\varepsilon < \varepsilon_L$  and decoheres immediately.

To quantify the degree of local and non-local entanglement between qubits  $Q_i$  and  $Q_j$ , we evaluate bipartite concurrence<sup>29</sup>  $C_{ij}$  from the density matrix obtained in the calculation (Fig. 4e). The concurrence takes  $C_{ij} = 1$  for maximally entangled states, while  $C_{ij} = 0$  for separable states. The concurrence  $C_{23}$  jumps to  $\approx 0.7$  when local entanglement is generated in  $S_{23}$ , but

the non-local entanglement immediately takes over as Q2 becomes disentangled from the system ( $C_{13} > 0.5$  and  $C_{12} = C_{23} = 0$ ). This clearly indicates that non-local entanglement is generated in the array of spin qubits, which is an essential step toward larger-scale quantum information processing. The calculation suggests oscillation of  $C_{ij}$  caused by the residual  $J_{12}$ , which implies that Q2 is entangled and disentangled from the system periodically. This oscillation should be totally suppressed when  $\varepsilon$  is made more negative to turn  $J_{12}$  off completely. On the other hand, this effect could be used to control entanglement of arbitrary qubit pairs, which should be demonstrated in more direct experimental investigation.

In the calculation, we assume the same Gaussian dephasing with  $T_2^* = 70$  ns for both the local ( $S_{23}$ - $T_{23}$ ) and non-local ( $S_{13}$ - $T_{13}$ ) evolutions, and we find the calculation consistent with the experimental data. This suggests that the local and non-local entanglements share the same decoherence mechanism, which is supposed to be the fluctuation of the nuclear spin bath in our device<sup>30</sup>. We therefore conclude that  $\Delta B_{23}$  and  $\Delta B_{13}$  have similar fluctuation spectra with no peculiar spatial correlation in the nuclear spin bath. Our result indicates that the coherence of the non-local entanglement can be maintained in larger-scale quantum computing devices, reinforcing the scalability of the QD-based architecture.

We have demonstrated coherent manipulation of local and non-local entanglement in a triple spin qubit device. We have analyzed the coherent evolution of entangled electron spins to obtain the three-spin spectrum, which enables precise control of three individual spin qubits and the exchange couplings between them. Our results not only demonstrate the feasibility of larger-scale quantum

information processing, but also suggest an unconventional approach to generate a non-locally entangled electron pair in solid state devices.

## Methods

**Measurement** The pulse sequences used in the experiment were generated by a Tektronix AWG70002 arbitrary waveform generator operated at 1 GSa/s. The output waveform was low-pass filtered by Mini-Circuits SBLP-300+ to adjust the rise time of the rapid adiabatic pulse used in the experiment as well as to filter out high-frequency noise. We find that the step response of the filter is well approximated by using the error function as  $\psi(t) = \frac{1}{2} \left( 1 + \text{erf} \left( \frac{t-t_0}{t_s} \right) \right)$  with  $t_s = 1.6$  ns. This effect is taken into account in the numerical calculations described below.

For the spin state initialization and readout, we adopted two different scenarios in the pulse sequences (see Extended Data Fig. 1). In the pulse sequence for the ESR and Rabi measurement (Figs. 1d, e), the spin states are initialized at point I near the (101)-(102) charge transition line in Fig. 1c, where an electron in an excited state can escape to a reservoir and the doubly occupied singlet state  $S_3$  is formed. Readout is performed at point  $M_0$ , where the relaxation time of two triplet states,  $|T_{+23}\rangle = |\uparrow_2\uparrow_3\rangle$  and  $|T_{-23}\rangle = |\downarrow_2\downarrow_3\rangle$ , is sufficiently long. However, the relaxation of the triplet state with anti-parallel spins,  $T_{23}$ , is too fast for single-shot readout because of the rapid state mixing with  $S_{23}$  by  $\Delta B_{23}$ <sup>31</sup>. Readout of the  $T_{23}$  component (used in Figs. 1f, 2, 3 and 4) is therefore performed at point  $M_1$  close to the triplet resonance point, where the relaxation of  $T_{23}$  is suppressed by the exchange coupling. Point  $M_0$  is instead used to let  $T_{23}$  relax and initialize the system to  $S_3$ , which is faster than the initialization at point I in our device.

The state  $|\sigma_1 S_3\rangle$  is loaded into (111) by using either slow (Figs. 1d, e) or rapid (Figs. 2-4) adiabatic passage<sup>7,32</sup>. In the former case, the detuning is displaced rapidly to cross the  $S_3-T_{+23}$  resonance line, and then ramped slowly (within  $1\mu s$ ) to  $\varepsilon = 0$ . During this adiabatic passage,  $|\sigma_1 S_3\rangle$  is loaded into the eigenstate of the local Zeeman field,  $|\sigma_1 \downarrow_2 \uparrow_3\rangle$ . Readout is performed after the detuning is pulsed back in reverse steps, where the  $|\sigma_1 \downarrow_2 \uparrow_3\rangle$  component returns to  $|\sigma_1 S_3\rangle$  in the (102) configuration while the  $|\sigma_1 \uparrow_2 \downarrow_3\rangle$ ,  $|\sigma_1 \uparrow_2 \uparrow_3\rangle$ , and  $|\sigma_1 \downarrow_2 \downarrow_3\rangle$  are unloaded to triplet components,  $|\sigma_1 T_{23}\rangle$  and  $|\sigma_1 T_{\pm 23}\rangle$ , staying in (111) due to Pauli spin blockade<sup>33</sup>. In the rapid adiabatic passage, the detuning is set to the target value so that  $|\sigma_1 S_3\rangle$  remains in the singlet state  $|\sigma_1 S_{23}\rangle$  if the target value is around  $\varepsilon = 0$ . For  $\varepsilon \neq 0$ , actual three-spin states prepared after the passage is subject to the target detuning value and the speed of the passage as discussed in the main text. When the detuning is pulsed back for readout,  $|\sigma_1 S_{23}\rangle$  returns to  $|\sigma_1 S_3\rangle$  while all the other triplet components remain spin-blocked.

For each single-shot readout of the spin state in the pulse cycles, the charge sensor signal in (102) is first measured for reference before the qubit operations. The final charge configuration after qubit operations is probed by integrating the sensor signal for  $4\mu s$ <sup>34</sup> and the change of the signal with respect to the reference one is recorded to subtract the slow drift of the background signal. The outcome is then mapped to either the singlet or one of the triplets. The identical single-shot measurement is repeated for  $N = 2000$  (Fig. 1e) or 200 (other figures) times to infer  $P_S$ <sup>34,35</sup>. Increasing  $N$  reduces the influence of projection noise in the readout process and improves the signal-to-noise ratio in the data. On the other hand, it increases the time required for overall data acquisition and broadens the spectrum of the nuclear bath fluctuation during the acquisition<sup>30,36</sup>.

We therefore kept  $N$  as small as possible to finish the data acquisition for Fig. 3a in only 22.7 seconds. To make a fluctuation spectrum homogeneous for the whole data set in a single acquisition, independent variables ( $t_{\text{evolve}}$  and  $\varepsilon$  in the case of Fig. 3a) are scanned consecutively to obtain single samples for each point and the whole scan is repeated  $N$  times. This results in the ensemble coherence time of  $T_2^* \sim 70$  ns in our experiment, that is almost an order of magnitude longer than the conventional value in GaAs<sup>7</sup>.

To find the ESR signals for each qubit,  $|\sigma_1 \downarrow_2 \uparrow_3\rangle$  was adiabatically loaded from  $|\sigma_1 S_3\rangle$ . To drive the ESR we applied a microwave burst of the duration  $t_{\text{burst}} = 1 \mu\text{s}$  to the gate electrode shared by the three QDs (horizontal fine gate in Fig. 1a). This leads to the mixing of  $|\sigma_1 \downarrow_2 \uparrow_3\rangle$  with  $|\sigma_1 \uparrow_2 \uparrow_3\rangle$  ( $|\sigma_1 \downarrow_2 \downarrow_3\rangle$ ), if qubit Q2 (Q3) is in resonance. The DC voltage applied to the shared gate was negatively offset during the microwave burst to prevent leakage of electrons to the reservoirs. We found two distinct ESR lines for Q2 and Q3 separated by  $\approx 8$  mT in the lower panel of Extended Data Fig. 2a with the effective  $g$ -factor  $|g| = 0.34$ . The ESR lines for Q1 and Q2 in the upper panel were taken by preparing  $|\downarrow_1 \uparrow_2 \sigma_3\rangle$  adiabatically loaded from  $|S_1 \sigma_3\rangle$ , revealing that the Zeeman field difference is  $\approx 18$  mT.

The Rabi oscillations in Fig. 1d were taken by repeating the single-shot measurement cycle with  $t_{\text{burst}}$  increased consecutively from 30 ns to  $1.8 \mu\text{s}$  in 60 steps within the laboratory time of 1.5 ms at the resonance conditions. The microwave frequency  $f_{\text{MW}}$  was ramped continuously over the frequency range of 80 MHz during the measurement, at a rate such that  $f_{\text{MW}}$  is increased by 2 kHz during the single measurement cycle of 1.5 ms. We then calculate the sliding Gaussian average of  $P_S$  first along the  $f_{\text{MW}}$  axis with the standard deviation of  $\sigma_f = 0.2$  MHz and then along

the  $t_{\text{burst}}$  axis with the standard deviation of  $\sigma_t = 30$  ns (Extended Data Fig. 2b). The averaged data at the resonance frequency were resampled for plotting with a  $t_{\text{burst}}$ -step of 60 ns. Similarly, the data in Fig. 4a were calculated by taking a Gaussian average along the detuning axis with  $\sigma_\varepsilon = 0.7$  GHz, while no averaging was performed along the  $t_{\text{evolve}}$  axis. Despite the low Rabi frequencies, we found sinusoidal oscillations damped with a Gaussian envelope that is expected only in the “fast” Rabi regime<sup>24</sup>. This is because our overall measurement time for sampling the Rabi oscillations is shorter than the typical correlation time of the nuclear bath fluctuation<sup>30,35,36</sup>.

**Model** We describe our TQD with the Hamiltonian

$$\mathcal{H} = H_t + H_\varepsilon + H_Z \quad (1)$$

$$\begin{aligned} H_t &= \sum_{\sigma_3} (t_{12} |S_1 \sigma_3\rangle \langle S_1 \sigma_3| + \text{h.c.}) + \sum_{\sigma_1} (t_{23} |\sigma_1 S_3\rangle \langle \sigma_1 S_3| + \text{h.c.}) \\ H_\varepsilon &= \sum_{\sigma_3} \frac{\varepsilon - \varepsilon_L}{2} |S_1 \sigma_3\rangle \langle S_1 \sigma_3| + \sum_{\sigma_1} \frac{-\varepsilon + \varepsilon_R}{2} |\sigma_1 S_3\rangle \langle \sigma_1 S_3| \\ H_Z &= \sum_i g \mu_B B_i \hat{s}_i^z, \end{aligned}$$

where  $S_1$  denotes the doubly occupied singlet state in QD 1 and  $\hat{s}_i^z$  is the  $z$  component of the spin operator. The local magnetic fields are given by  $B_1 = B_{\text{ext}} - \Delta B_{12}/(|g|\mu_B)$ ,  $B_2 = B_{\text{ext}}$ , and  $B_3 = B_{\text{ext}} + \Delta B_{23}/(|g|\mu_B)$  (note that  $\Delta B_{ij}$  is defined in units of energy). To explain the experimental results, we find it necessary to take into account the detuning-dependent inter-dot tunnel couplings. Here we adopted phenomenological functions of the forms  $t_{12} = t_L (1 - \text{erf}(\frac{\varepsilon - \varepsilon_L}{w}))$  and  $t_{23} = t_R (1 - \text{erf}(\frac{-\varepsilon + \varepsilon_R}{w}))$  with  $w/h = 60.0$  GHz, which are similar to those used in the previous TQD experiments<sup>16,23,28</sup>.

The Hamiltonian in Eq. 1 is diagonalized using the program QuTiP<sup>37</sup>. To fit the experimental

data in Fig. 3 with calculated energy gaps, we also take into account the  $S_1$ - $T_{+12}$  and  $S_3$ - $T_{+23}$  resonance points which appear as faint vertical lines at  $(\varepsilon_L - \varepsilon)/2 = |g|\mu_B(B_1 + B_2)/2$  and  $(\varepsilon - \varepsilon_R)/2 = |g|\mu_B(B_2 + B_3)/2$  for  $t_{\text{evolve}} > 100$  ns. These constraints together with the spectral lines in Fig. 3d are sufficient to derive all the unknown parameters in Eq. 1. We also confirmed that the derived energy scale of the detuning axis agrees with the photon-assisted tunneling observed in a separate experiment (data not shown). The calculated eigenenergies for the derived parameters are shown in Extended Data Fig. 3a and Fig. 1b as well as the exchange couplings in Extended Data Fig. 3b.

The coherent evolution of the system is calculated by numerically solving the Lindblad master equation. The detuning  $\varepsilon$  is changed as a function of time to simulate the approximate pulse waveforms used in the experiment. To describe fast dephasing between different charge states, we adopted the collapse operators,  $\sqrt{2\gamma}|S_1\sigma_3\rangle\langle S_1\sigma_3|$  and  $\sqrt{2\gamma}|\sigma_1S_3\rangle\langle\sigma_1S_3|$ , with  $\gamma = 0.5$  GHz being the dephasing rate. The ensemble dephasing effect is taken into account separately after the numerical calculation. The calculated evolutions are convoluted with a Gaussian kernel with  $\sigma_\varepsilon = 0.7$  GHz being the standard deviation of  $\varepsilon$ . The oscillations are then Gaussian decayed with  $T_2^* = 70$  ns. We note that both charge and spin relaxation processes are insignificant on our experimental time scales. Finally, we assume a readout fidelity of 0.8 for triplet outcomes.

The calculation suggests that the superposition of  $|\uparrow_1\uparrow_2\downarrow_3\rangle$  and  $|T_{12}\uparrow_3\rangle$  is likely to be realized when  $|\uparrow_1 S_{23}\rangle$  is loaded to  $\varepsilon \approx \varepsilon_L$  (see Extended Data Fig. 4a, b). The loaded state starts precession in the Bloch sphere spanned by  $|\uparrow_1\uparrow_2\downarrow_3\rangle$  and  $|T_{12}\uparrow_3\rangle$ , thus periodically approaching the W state,  $|W\rangle = \sqrt{\frac{1}{3}}|\uparrow_1\uparrow_2\downarrow_3\rangle + \sqrt{\frac{2}{3}}|T_{12}\uparrow_3\rangle$ . Since the state fidelity strongly depends on the

adiabacity of the operation pulse and the TQD parameters, quantitative evaluation of the fidelity requires further experimental investigation. Nevertheless, our result suggests that fidelity as high as  $\sim 90\%$  is within experimental reach by adjusting the adiabacity and suppressing the state leakage.

## References

1. Einstein, A., Podolsky, B. & Rosen, N. Can quantum-mechanical description of physical reality be considered correct? *Physical Review* **47**, 777–780 (1935).
2. Bell, J. S. On the einstein-podolsky-rosen paradox. *Physics* **1**, 195–200 (1964).
3. Aspect, A., Grangier, P. & Roger, G. Experimental realization of Einstein-Podolsky-Rosen-Bohm Gedanken experiment: A new violation of Bell’s inequalities. *Physical Review Letters* **49**, 91–94 (1982).
4. Hensen, B. *et al.* Loophole-free Bell inequality violation using electron spins separated by 1.3 kilometres. *Nature* (2015). URL <http://www.nature.com/doifinder/10.1038/nature15759.1508.05949>.
5. Bennett, C. H. & DiVincenzo, D. P. Quantum information and computation. *Nature* **404**, 247 (2000).
6. Gehring, T. *et al.* Implementation of continuous-variable quantum key distribution with composable and one-sided-device-independent security against coherent attacks. *Nat Commun* **6**, 1–7 (2015). URL <http://dx.doi.org/10.1038/ncomms979510.1038/ncomms9795>.

7. Petta, J. R. *et al.* Coherent manipulation of coupled electron spins in semiconductor quantum dots. *Science* **309**, 2180–2184 (2005).
8. Brunner, R. *et al.* Two-Qubit Gate of Combined Single-Spin Rotation and Interdot Spin Exchange in a Double Quantum Dot. *Physical Review Letters* **107**, 146801 (2011). URL <http://link.aps.org/doi/10.1103/PhysRevLett.107.146801>.
9. Nowack, K. C. *et al.* Single-shot correlations and two-qubit gate of solid-state spins. *Science (New York, N.Y.)* **333**, 1269–72 (2011).
10. Braakman, F., Barthelemy, P., Reichl, C., Wegscheider, W. & L.M.K., V. Long-distance coherent coupling in a quantum dot array. *Nature nanotechnology* **8**, 432–7 (2013).
11. Baart, T. A., Fujita, T., Reichl, C., Wegscheider, W. & Vandersypen, L. M. K. Coherent spin-exchange via a quantum mediator 1–23 (2016). URL <http://arxiv.org/abs/1603.03433>.
12. Koppens, F. H. L. *et al.* Driven coherent oscillations of a single electron spin in a quantum dot. *Nature* **442**, 766–771 (2006).
13. Nowack, K. C., Koppens, F. H. L., Nazarov, Y. V. & Vandersypen, L. M. K. Coherent control of a single electron spin with electric fields. *Science* **318**, 1430–1433 (2007).
14. Pioro-Ladrière, M. *et al.* Electrically driven single-electron spin resonance in a slanting Zeeman field. *Nature Physics* **4**, 776–779 (2008).

15. Laird, E. A. *et al.* Coherent spin manipulation in an exchange-only qubit. *Physical Review B* **82**, 075403 (2010). URL <http://link.aps.org/doi/10.1103/PhysRevB.82.075403>.

16. Gaudreau, L. *et al.* Coherent control of three-spin states in a triple quantum dot. *Nature Physics* **8**, 54–58 (2011). URL <http://www.nature.com/doifinder/10.1038/nphys2149>.

17. Amaha, S. *et al.* Two- and three-electron pauli spin blockade in series-coupled triple quantum dots. *Physical Review Letters* **110**, 1–5 (2013).

18. Loss, D. & DiVincenzo, D. P. Quantum computation with quantum dots. *Physical Review A* **57**, 120–126 (1998). URL <http://link.aps.org/doi/10.1103/PhysRevA.57.120>.

19. Veldhorst, M. *et al.* A two-qubit logic gate in silicon. *Nature* **526**, 410–414 (2015). URL <http://www.nature.com/doifinder/10.1038/nature15263>.

20. Shulman, M. D. *et al.* Demonstration of entanglement of electrostatically coupled singlet-triplet qubits. *Science (New York, N.Y.)* **336**, 202–5 (2012).

21. Mehl, S. & DiVincenzo, D. P. Simple operation sequences to couple and interchange quantum information between spin qubits of different kinds. *Physical Review B* **92**, 115448 (2015).

22. Medford, J. *et al.* Self-consistent measurement and state tomography of an exchange-only spin qubit. *Nature nanotechnology* **8**, 654–9 (2013).

23. Eng, K. *et al.* Isotopically enhanced triple-quantum-dot qubit. *Science Advances* e1500214 (2015).

24. Yoneda, J. *et al.* Fast Electrical Control of Single Electron Spins in Quantum Dots with Vanishing Influence from Nuclear Spins. *Physical Review Letters* **113**, 267601–1–5 (2014). URL <http://link.aps.org/doi/10.1103/PhysRevLett.113.267601>.

25. Yoneda, J. *et al.* Robust micromagnet design for fast electrical manipulations of single spins in quantum dots. *Applied Physics Express* **8**, 084401 (2015).

26. Noiri, A. *et al.* Coherent electron-spin-resonance control of three individual spins in a quantum dot array. (*to appear in Appl. Phys. Lett.*) .

27. Trifunovic, L. *et al.* Long-distance spin-spin coupling via floating gates. *Physical Review X* **2**, 011006 (2012).

28. Medford, J. *et al.* Quantum-Dot-Based Resonant Exchange Qubit. *Physical Review Letters* **111**, 050501 (2013). URL <http://link.aps.org/doi/10.1103/PhysRevLett.111.050501>.

29. Hill, S. & Wootters, W. K. Entanglement of a Pair of Quantum Bits. *Phys. Rev. Lett.* **78**, 5022–5025 (1997).

30. Delbecq, M. R. *et al.* Quantum dephasing in a gated GaAs triple quantum dot due to non-ergodic noise. *Phys. Rev. Lett.* **116**, 046802 (2016).

31. Barthel, C. *et al.* Relaxation and readout visibility of a singlet-triplet qubit in an Overhauser field gradient. *Physical Review B* **85**, 035306 (2012). URL <http://link.aps.org/doi/10.1103/PhysRevB.85.035306>.

32. Taylor, J. *et al.* Relaxation, dephasing, and quantum control of electron spins in double quantum dots. *Physical Review B* **76**, 035315 (2007). URL <http://link.aps.org/doi/10.1103/PhysRevB.76.035315>.

33. Ono, K., Austing, D. G., Tokura, Y. & Tarucha, S. Current rectification by Pauli exclusion in a weakly coupled double quantum dot system. *Science* **297**, 1313–1317 (2002).

34. Barthel, C. *et al.* Fast sensing of double-dot charge arrangement and spin state with a radio-frequency sensor quantum dot. *Physical Review B* **81**, 161308(R) (2010).

35. Barthel, C., Reilly, D., Marcus, C., Hanson, M. & Gossard, A. Rapid Single-Shot Measurement of a Singlet-Triplet Qubit. *Physical Review Letters* **103**, 160503 (2009). URL <http://link.aps.org/doi/10.1103/PhysRevLett.103.160503>.

36. Reilly, D. J. *et al.* Measurement of Temporal Correlations of the Overhauser Field in a Double Quantum Dot. *Physical Review Letters* **101**, 236803 (2008). URL <http://link.aps.org/doi/10.1103/PhysRevLett.101.236803>.

37. Johansson, J. R., Nation, P. D. & Nori, F. QuTiP 2: A Python framework for the dynamics of open quantum systems. *Computer Physics Communications* **184**, 1234–1240 (2013). URL <http://dx.doi.org/10.1016/j.cpc.2012.11.019>. 1211.6518.

**Acknowledgements** We thank S. Bartlett and P. Stano for fruitful discussions. We thank RIKEN CEMS Emergent Matter Science Research Support Team and Microwave Research Group in Caltech for technical assistance. Part of this work was supported financially by the Funding Program for World-Leading Innovative R&D on Science and Technology (FIRST) from the Japan Society for the Promotion of Science, ImPACT Program of Council for Science, Technology and Innovation and IARPA project Multi-Qubit Coherent Operations through Copenhagen University, the Grant-in-Aid for Research Young Scientists B, and RIKEN Incentive Research Project. T.O. acknowledges support from Toyota Physical & Chemical Research Institute Scholars, Yazaki Memorial Foundation for Science and Technology Research Grant, Japan Prize Foundation Research Grant, Advanced Technology Institute Research Grant, and the Murata Science Foundation Research Grant. A.D.W. and A.L. greatfully acknowledge support from Mercur Pr2013-0001, BMBF Q.Com-H 16KIS0109, TRR160, and DFH/UFA CDFA-05-06.

**Author Contributions** T.N. and S.T. planned the project. A.L. and A.D.W grew the heterostructure and T.N. fabricated the device. T.N. conducted the experiment with the assistance of M.R.D, T.O., J.Y. and A.N.; T.N. analyzed the data and performed numerical calculations with the help of M.R.D., S.A., J.Y., and T.O. All authors discussed the results and commented on the manuscript. The project was supervised by S.T.

**Author Information** Reprints and permissions information is available at [www.nature.com/reprints](http://www.nature.com/reprints). The authors declare no competing financial interests. Correspondence should be addressed to T.N. (nakajima.physics@icloud.com) or S.T. (tarucha@ap.t.u-tokyo.ac.jp).

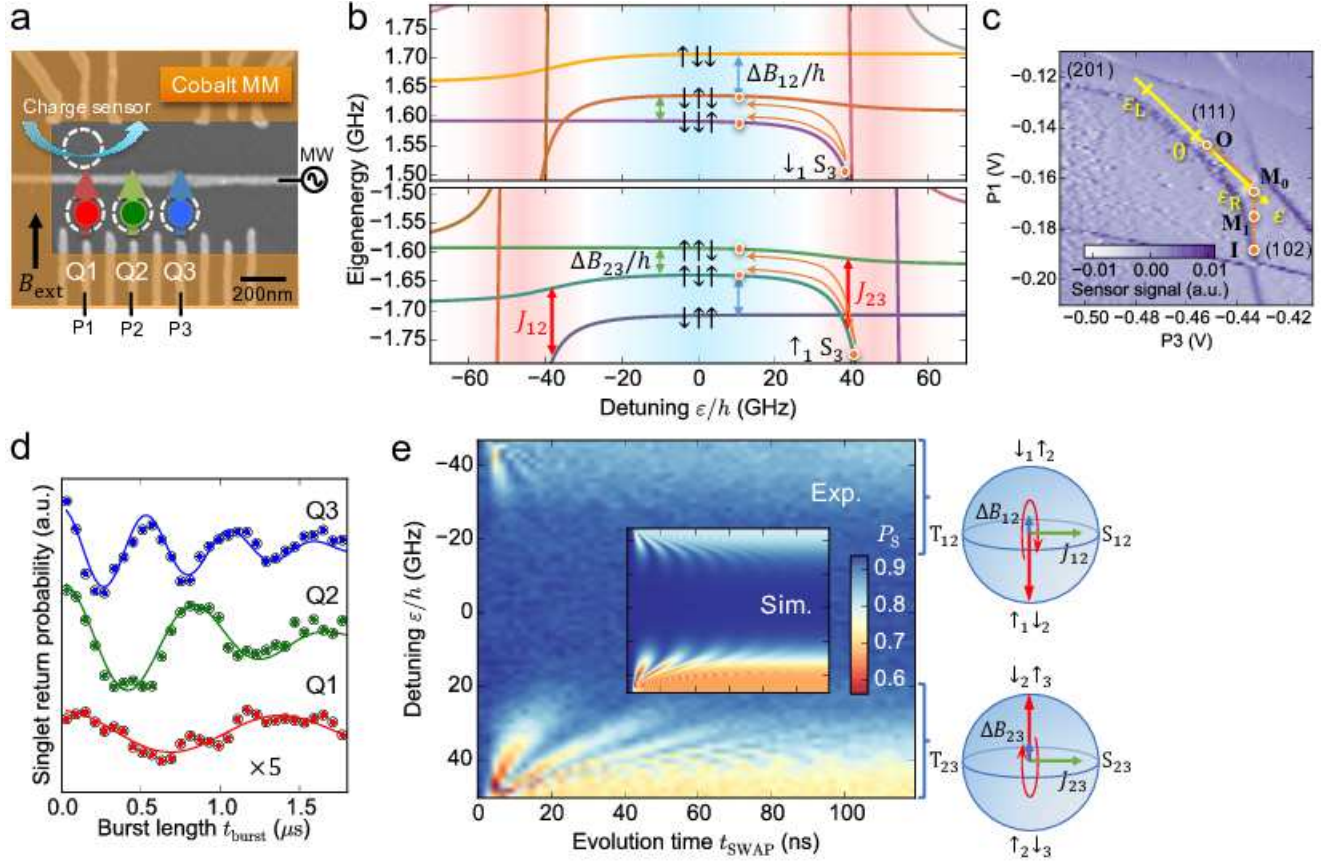


**Figure 1 Experimental implementation of three spin qubits.** **a**, Schematic of a TQD device similar to the one measured. Qubits Q1-3 are encoded in single electron spins in each QD. The cobalt micromagnet deposited on a calixarene insulation layer induces the difference of the local Zeeman field  $\Delta B_{12}$  ( $\Delta B_{23}$ ) between Q2 and Q1 (Q3 and Q2). **b**, Energy diagram of the three-spin states calculated with the parameters derived from the Fourier transform spectroscopy in Fig. 3. Only the states with  $S_z = \pm 1/2$  are shown here (See Extended Data Fig. 3 for the  $S_z = \pm 3/2$  branches). **c**, Charge stability diagram of the TQD obtained by differentiating the rf-reflectometry signal of the nearby QD charge sensor. **d**, Rabi oscillations of Q1 (magnified fivefold), Q2, and Q3 driven by the applica-

tion of the microwave burst of length  $t_{\text{burst}}$  at  $B_{\text{ext}} = 0.7$  T. **e**, SWAP operations between  $|\uparrow_1\downarrow_2\uparrow_3\rangle$  and  $|\downarrow_1\uparrow_2\uparrow_3\rangle$  ( $|\sigma_1\downarrow_2\uparrow_3\rangle$  and  $|\sigma_1\uparrow_2\downarrow_3\rangle$ ) driven by brief excursions to negative (positive) detuning. The inset shows the calculation result. The oscillation amplitude at  $\varepsilon < 0$  is smaller than that at  $\varepsilon > 0$  because the SWAP signal between Q1 and Q2 is visible only for the fraction with  $\sigma_1 = \uparrow$  in the density matrix  $\rho_0$ .

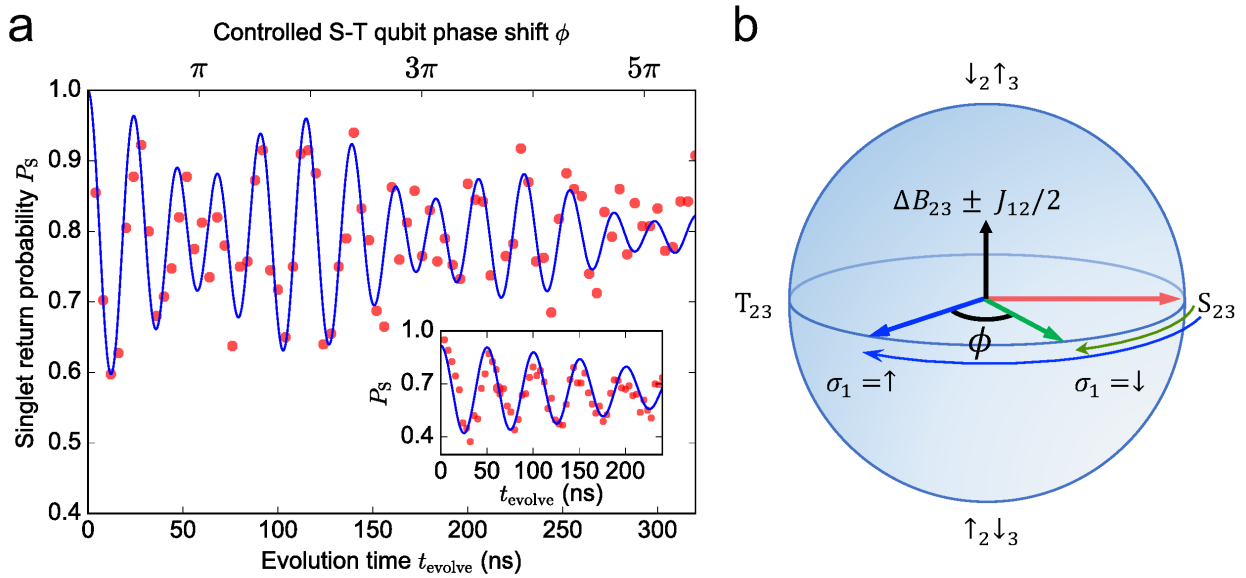


**Figure 2 Coherent oscillations between  $S_{23}$  and  $T_{23}$  phase-controlled by Q1.** **a**, Experimental data (red circles) with finite  $J_{12}$  and those with negligibly small  $J_{12}$  (inset) taken at  $\varepsilon = 0$ . The blue curves are fits to the data with the function  $P_s = \beta\{\alpha \cos(2\pi f_{\uparrow}t) + (1 - \alpha) \cos(2\pi f_{\downarrow}t)\}e^{-(t/T_2^*)^2} + (1 - \beta)$ , where the frequency shift between  $f_{\uparrow} = 43.5$  MHz and  $f_{\downarrow} = 35.0$  MHz in the main panel is given by  $J_{12}/h$  while  $f_{\uparrow} - f_{\downarrow} \approx 0$  in the inset. Note that the value of  $\Delta B_{23}/h = \frac{f_{\uparrow}+f_{\downarrow}}{2}$  in the inset is different from the one in the main panel due to the nuclear spin fluctuation. **b**, Schematic representation of the  $S_{23}$ - $T_{23}$  oscillation in the Bloch sphere spanned by the two-spin eigenstates  $|\downarrow_2\uparrow_3\rangle$  and  $|\uparrow_2\downarrow_3\rangle$ . The phase shift  $\phi$  is

controlled by the state of Q1.

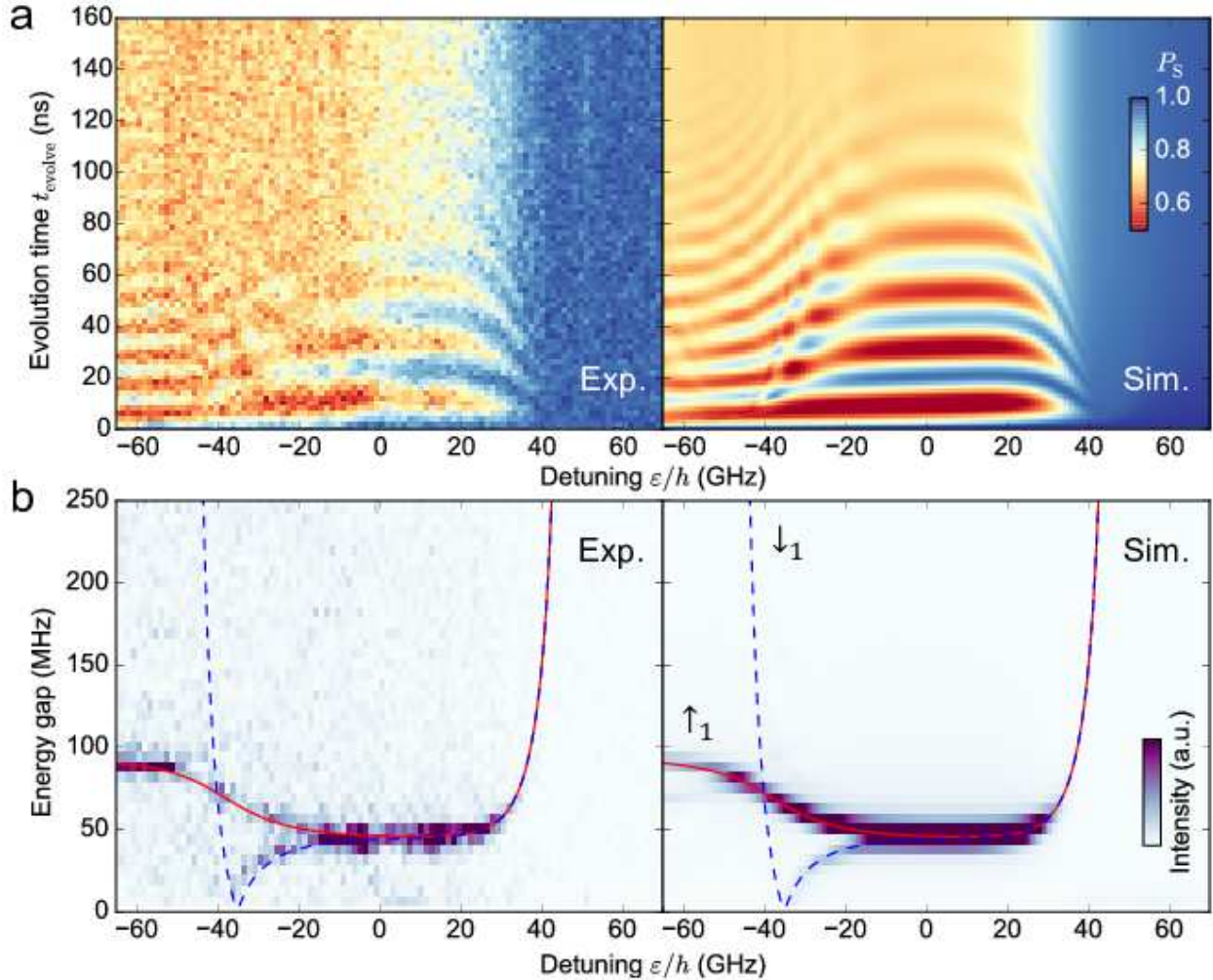


**Figure 3 Pulsed Fourier transform spectroscopy of the triple spin qubit system.**

**a**, Measured (Exp.) and calculated (Sim.) coherent evolution of the three-spin state. The spins are rapidly loaded to (111) from a doubly occupied singlet state in the right QD,  $|\sigma_1 S_3\rangle$ , left to evolve for  $t_{\text{evolve}}$ , and then projected back to the singlet state for spin blockade measurement. The calculation is performed with the inter-dot tunnel couplings  $t_L/h = 0.75$  GHz and  $t_R/h = 0.75$  GHz, the detuning values of (201)-(111) and (111)-(102)

resonances  $\varepsilon_L/h = -46$  GHz and  $\varepsilon_R/h = 46$  GHz, and the local Zeeman field differences  $\Delta B_{12}/h = 70$  MHz and  $\Delta B_{23}/h = 45$  MHz (see Methods), that are derived from the fitting in **b**. **b**, Fast Fourier transform of the data in **a** for each detuning value. Red solid lines (blue dashed lines) represent the energy gap between the two branches of  $|\uparrow_1\uparrow_2\downarrow_3\rangle$  and  $|\uparrow_1\downarrow_2\uparrow_3\rangle$  ( $|\downarrow_1\uparrow_2\downarrow_3\rangle$  and  $|\downarrow_1\downarrow_2\uparrow_3\rangle$ ) near  $\varepsilon = 0$  as shown in Fig. 1b, which is accessed by a state loaded from  $|\uparrow_1 S_3\rangle$  ( $|\downarrow_1 S_3\rangle$ ) in  $\rho_0$ .

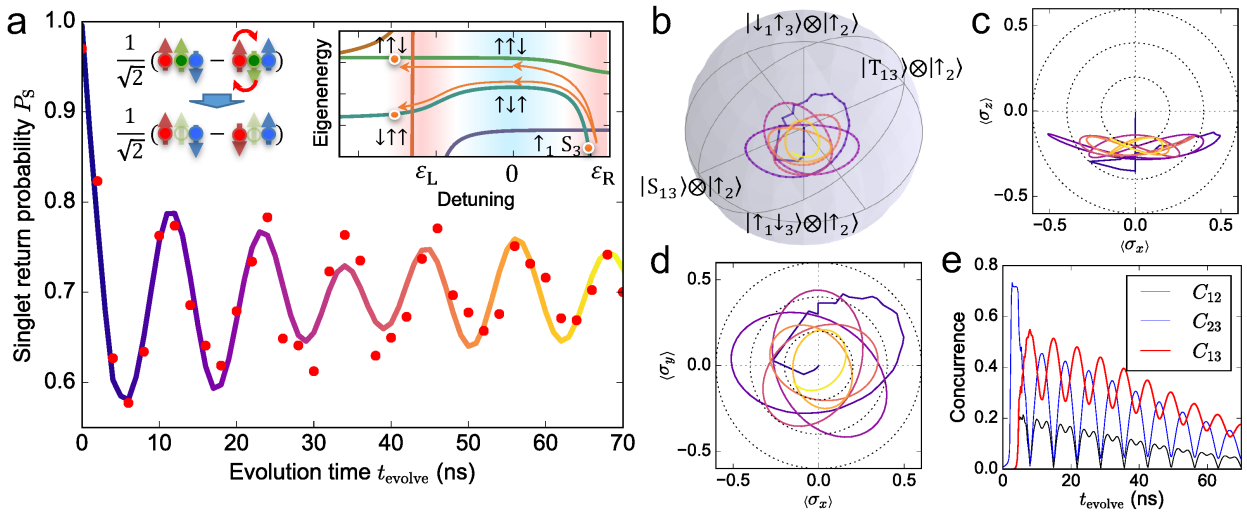
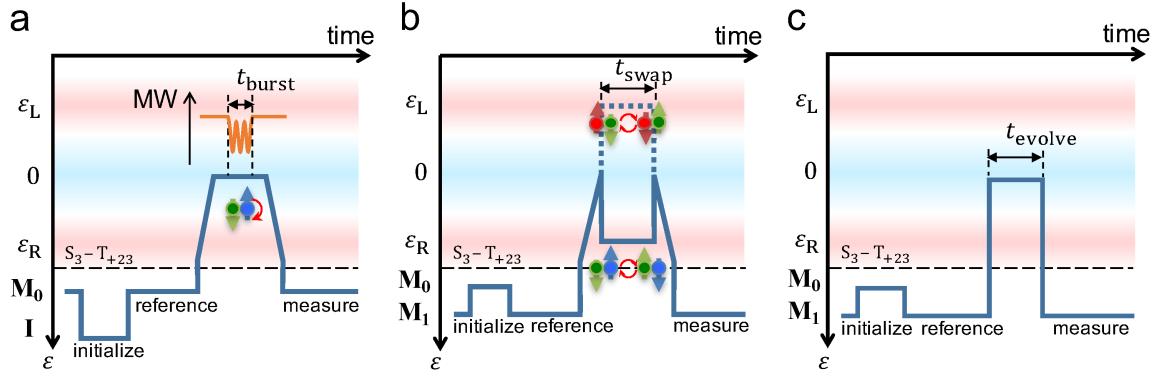
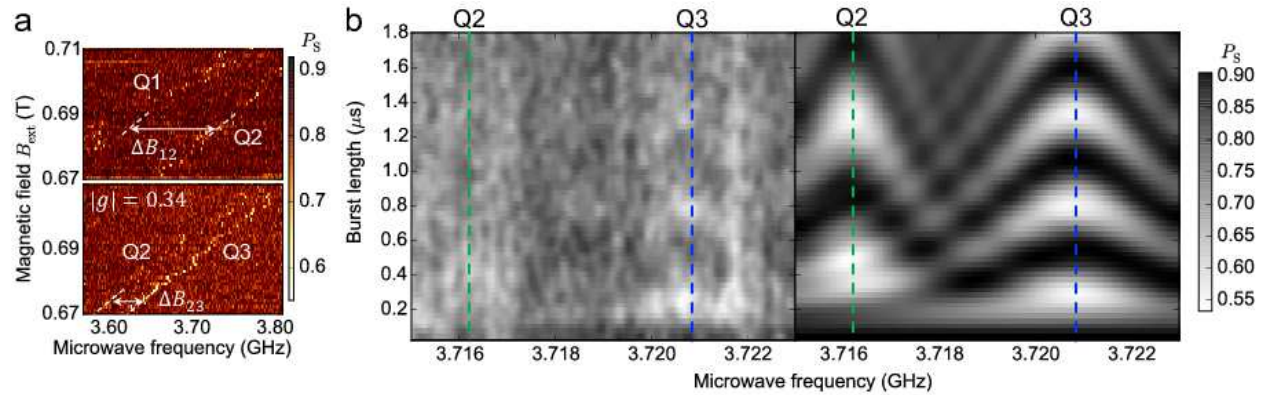


**Figure 4 Coherent evolution of the nonlocally entangled spin state.** **a**, Measured (red circles) and calculated (solid line) coherent oscillations at  $\varepsilon/h = -58$  GHz. The  $|\uparrow\downarrow\uparrow\rangle$  component in the nearest neighbor entanglement  $|\uparrow_1\rangle\otimes|S_{23}\rangle = \frac{1}{\sqrt{2}}(|\uparrow\uparrow\downarrow\rangle - |\uparrow\downarrow\uparrow\rangle)$  is adiabatically transferred to  $|\downarrow\uparrow\uparrow\rangle$  with the help of the exchange coupling  $J_{12}$  during the rapid ramping pulse, resulting in the nonlocally entangled state  $|\uparrow_2\rangle\otimes|S_{13}\rangle = \frac{1}{\sqrt{2}}(|\uparrow\uparrow\downarrow\rangle - |\downarrow\uparrow\uparrow\rangle)$  as shown in the inset. **b**, Trajectory of the calculated Bloch vector in the reduced Hilbert space spanned by  $|\uparrow_1\downarrow_3\rangle\otimes|\uparrow_2\rangle$  and  $|\downarrow_1\uparrow_3\rangle\otimes|\uparrow_2\rangle$ . The color represents the evolution time as

shown by the calculated curve in **a**. **c, d**, The trajectory of the Bloch vector projected onto the  $x$ - $z$  plane (**c**) and  $x$ - $y$  plane (**d**). **e**, Bipartite concurrence  $C_{ij}$  for  $Q_i$  and  $Q_j$  calculated by tracing out the  $Q_k$  ( $k \neq i, j$ ) subspace.

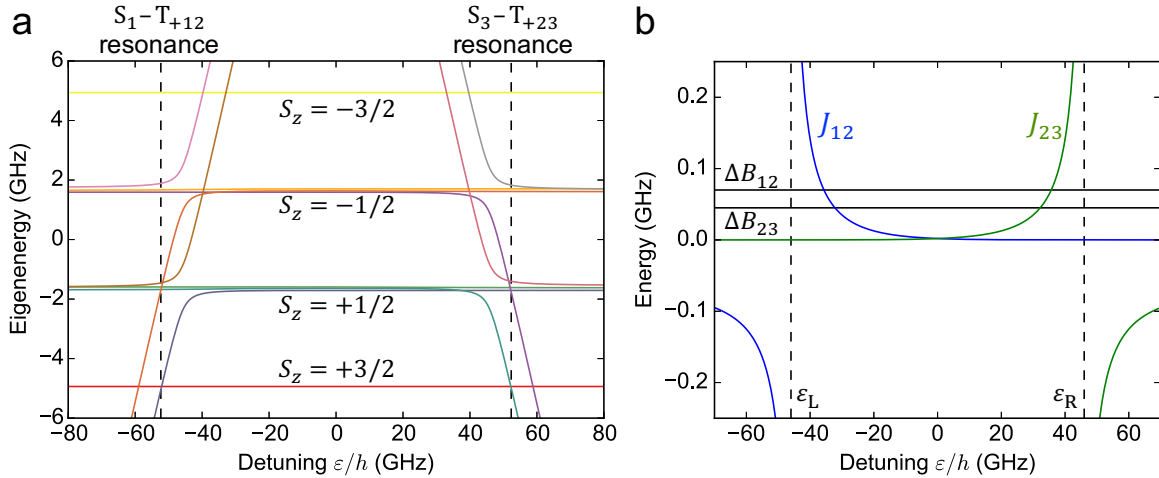


**Extended Data Figure 1** Pulse sequences used in the experiment. **a**, Pulse sequence used in the ESR and Rabi measurements in Figs. 1d and 1e. **b**, Sequence used in the SWAP measurement in Fig. 1f. **c**, Sequence used in the measurement of the coherent evolution of the entangled states in Figs. 2, 3 and 4.



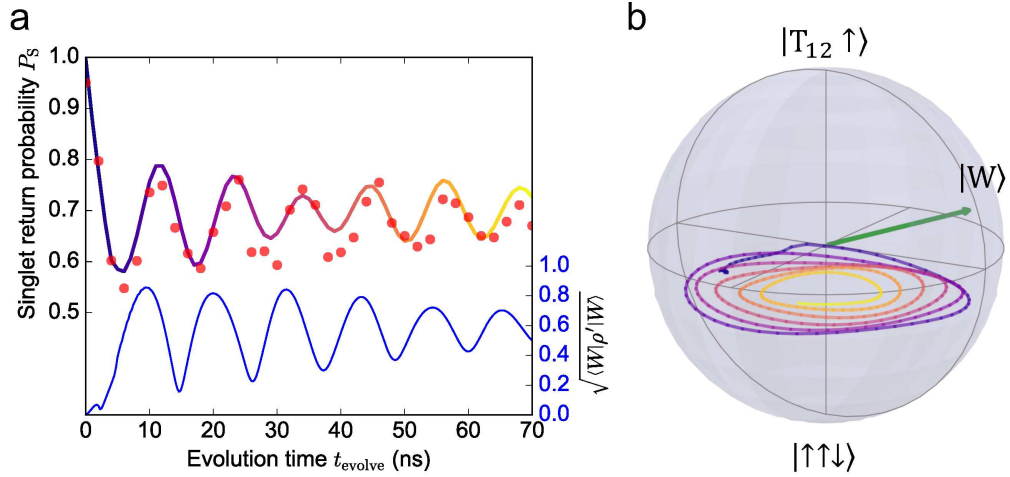
**Extended Data Figure 2** ESR and Rabi oscillations of the spin qubits. **a**, ESR signals measured as a function of  $B_{\text{ext}}$  and the microwave frequency for Q1 and Q2 (upper

panel) and Q2 and Q3 (lower panel). Note that the resonance frequency of Q2 in the upper panel is shifted from the one in the lower panel because the gate bias conditions (and consequently the local Zeeman field) are slightly changed to improve the visibility of the spin blockade signal near the (111)-(201) charge transition. **b**, Rabi oscillations of Q2 and Q3 with microwave frequency detuning. The left panel shows the experimental data where  $P_S$  is derived from 60 consecutive sweeps of  $t_{\text{burst}}$  and then smoothed by taking a sliding Gaussian average. Calculated chevron patterns for derived ESR frequencies and Rabi frequencies are shown in the right panel. The Rabi oscillation for Q2 (Q3) in Fig. 1d in the main text is extracted from the data along the green (blue) dashed line.



**Extended Data Figure 3 Energy diagram of the three-spin states.** **a**, All of the eight three-spin energy eigenstates calculated from Eq. 1 are shown. Expanded views of the  $S_z = \pm 1/2$  branches are shown in Fig. 1c. The detuning values of the singlet-triplet resonance points near the (201)-(111) and (111)-(102) charge transitions are shown with dashed lines. **b**, The calculated exchange couplings  $J_{12} = t_{12}^2/(\varepsilon - \varepsilon_L)$  and  $J_{23} = t_{23}^2/(\varepsilon_R -$

$\varepsilon$ ) determined from the fitting to the experimental data.



**Extended Data Figure 4 Coherent evolution of the entangled spin state near  $\varepsilon = \varepsilon_L$ .**

**a**, Measured (red circles) and calculated (upper solid line) coherent oscillations at  $\varepsilon/h = -54$  GHz. The blue solid line shows the fidelity of the W state inferred from the calculation. The state leakage to (102) and (201) charge configurations is removed by normalizing the density matrix  $\rho$  as  $\rho' = \rho / (\text{Tr}(\rho) - \langle \sigma_1 S_3 | \rho | \sigma_1 S_3 \rangle - \langle S_1 \sigma_3 | \rho | S_1 \sigma_3 \rangle)$ . **b**, Trajectory of the calculated Bloch vector in the reduced Hilbert space spanned by  $|T_{12} \uparrow\rangle$  and  $|\uparrow_1 \uparrow_2 \downarrow_3\rangle$ . A green arrow represents the W state.